Riluzole Preserves Brain Endothelial Integrity in Ischemic Stroke via SLC7A11-Dependent GPX4 and HIF-1α/VEGFA Signaling

Haipeng Wang [a], Ying Feng [a, b], Wei Jiang [a], Han Wang [a], Ruolin Zhang [a], Guangqiang Li [a], Chao Duan [a, b], Yuneng Zhou [a], Wendai Bao [a], Ke Shui [a], Min Zhang [a], Zhibing Ai [e], Xin Yang [f], Peiyang Zhou [c#], Zhiqiang Dong [a, b, d#]

[a]College of Biomedicine and Health, College of Life Science and Technology, Huazhong Agricultural University, Wuhan 430070, Hubei, China

[b]Hubei Clinical Research Center of Central Nervous System Repair and Functional Reconstruction, Taihe Hospital, Hubei University of Medicine, Shiyan 442000, Hubei, China

[c]Department of Neurology, Xiangyang No.1 People's Hospital, Hubei University of Medicine, Xiangyang 441000, Hubei, China

[d]Hubei Jiangxia Laboratory, Wuhan 430207, Hubei, China

[e]Department of Neurology, Taihe Hospital, Hubei University of Medicine, Shiyan 442000, Hubei, China

[f]Department of Electrical and Electronic Engineering, School of Engineering Cardiff University, Cardiff CF24 3AA, UK

[#]Corresponding author: Zhiqiang Dong: dongz@mail.hzau.edu.cn; Peiyang Zhou: zhoupeiyang@126.com

ABSTRACT

Riluzole, an FDA-approved neuroprotective agent, was investigated for its therapeutic potential in ischemic stroke. Transcriptomic profiling of human brain microvascular endothelial cells (hBMECs) subjected to oxygen-glucose deprivation/reperfusion (OGD/R) identified a pivotal role for the cystine/glutamate antiporter SLC7A11. We found that riluzole activates SLC7A11, thereby triggering a dual protective mechanism: it strengthens cellular antioxidant capacity by upregulating GPX4 while simultaneously enhancing proangiogenic signaling through the HIF-1α/VEGFA pathway. Consequently, riluzole attenuated OGD/R-induced endothelial injury and, in a mouse stroke model, reduced blood–brain barrier disruption and improved neurological outcomes. Our study reveals a previously unrecognized cerebrovascular protective mechanism of riluzole, establishing SLC7A11 as its key mediator. This SLC7A11-dependent dual-pathway action

represents a substantive advance in understanding riluzole's therapeutic biology beyond its established roles in the central nervous system.

KEYWORDS

Riluzole, SLC7A11, GPX4, HIF-1α, VEGFA, MCAO/R

1. Introduction

Ischemic stroke (IS) is a leading cause of mortality and long-term disability worldwide, with an especially high incidence in China, where it accounts for over 80% of all stroke cases **[1-5]**. The pathophysiology of IS involves the abrupt interruption of cerebral blood flow, leading to neuronal necrosis, glial activation, and blood-brain barrier (BBB) disruption. Among these, the structural and functional integrity of the BBB plays a central role in determining the extent of post-stroke injury and the success of tissue recovery **[6]**.

Brain microvascular endothelial cells (BMECs), which constitute the core component of the BBB, are critical for maintaining neurovascular homeostasis **[7,8]**. Unlike peripheral endothelial cells, BMECs are uniquely specialized to support selective permeability, immune surveillance, and neurovascular signaling within the central nervous system **[9]**. However, they are highly vulnerable to ischemia-reperfusion (I/R)-induced oxidative stress, calcium overload, and inflammation, representing one of the earliest cellular targets in stroke **[10-12]**. Dysfunctional BMECs not only compromise BBB integrity but also exacerbate cerebral edema, neuroinflammation, and secondary neuronal injury **[13]**.

Protecting BMECs from I/R-induced injury and promoting their functional recovery have thus emerged as important therapeutic goals in IS research. Various pharmacological agents, including antioxidants and anti-inflammatory compounds derived from both synthetic drugs and traditional Chinese medicine, have shown promise in ameliorating BMEC injury **[6,14-18]**.

Recent evidence suggests that ferroptosis—a form of regulated cell death characterized by iron-dependent lipid peroxidation—plays a pivotal role in endothelial cell injury during I/R **[19]**. A key regulator of ferroptosis is SLC7A11, a cystine/glutamate antiporter that maintains intracellular redox balance by promoting glutathione synthesis. However, the role of SLC7A11 in BMECs under ischemic conditions and its therapeutic modulation remains poorly understood.

Riluzole, a glutamate release inhibitor approved by the U.S. Food and Drug Administration for the treatment of amyotrophic lateral sclerosis (ALS), has been reported to exhibit neuroprotective

effects in multiple CNS disorders, including stroke. Intriguingly, riluzole has also been implicated in the upregulation of SLC7A11 expression, although its mechanisms of action in cerebrovascular endothelial cells have not been fully elucidated.

In this study, using a human brain microvascular endothelial cell (hBMEC) model of oxygen-glucose deprivation/reperfusion (OGD/R), we investigated the transcriptomic and functional changes induced by ischemic injury. We identified SLC7A11 as a key downregulated gene following OGD/R and demonstrated that its overexpression protected hBMECs against oxidative stress, preserved angiogenic capacity, and enhanced antioxidant signaling. Moreover, we assessed the therapeutic potential of riluzole in both hBMECs and mouse BEND3 endothelial cells. The results revealed that riluzole dually activates the SLC7A11/GPX4 antioxidant axis and the SLC7A11/HIF-1α/VEGFA pro-angiogenic pathway, which was further corroborated by its neuroprotective effect in MCAO/R mice. Collectively, our findings uncover a novel endothelial-protective mechanism of riluzole and offer new insights into pharmacologically targeting the BBB in ischemic stroke.

2. Materials and methods

2.1. Cell culture

HBMECs were purchased from ScienCell (Carlsbad, CA, USA) and have been verified by CD31 immunofluorescence assay **(Fig. S1)**. BEND3 cells were procured from Procell Life Science & Technology Co., Ltd. HBMECs were cultured in RPMI-1640 complete medium (86% RPMI-1640 (Servicebio, Wuhan, Hubei, China) + 10% FBS (Fetal Bovine Serum, VivaCell, Shanghai, China) + 1% P/S (Penicillin-Streptomycin Solution, Biosharp, Hefei, Anhui, China) + 1% NEAA (Non-essential amino acid, Gibco, Paisley, Scotland, UK) + 1% AA (Amino acid, Sigma-Aldrich, St Louis, MO, USA) + 1% Vitamin (Procell, Wuhan, Hubei, China)), BEND3 cells were cultured in DMEM complete medium (89% DMEM (Procell) + 10% FBS (VivaCell) + 1% P/S (Biosharp)), and 293T cells were cultured in DMEM complete medium (same as BEND3 cells). The above cells were cultured in 5% CO_2 at 37°C in the dark.

2.2. OGD/R model preparation

Spread BMECs into cell culture dishes or plates in advance, and OGD/R experiments can be done when the cells are adherent to the wall and the degree of fusion is 70%-80%. The exploration of OGD/R conditions for hBMEC and BEND3 is detailed in **Fig. S2 and S3**, where the hBMEC

OGD (0% O_2, 5% CO_2, 95% N_2) treatment time is 4 h and the reoxygenation time is 24 h. The OGD treatment time for BEND3 (1% O_2, 5% CO_2, 94% N_2) is 2 h, and the reoxygenation time is 24 h. The medium used during OGD treatment was DMEM sugar-free medium (Procell).

2.3. Cell viability assay

BMECs were inoculated into 96-well plates (5×10^3 cells per well) for OGD/R or riluzole treatment. Riluzole and Ferrostatin-1 (Fer-1) was prepared as a 100 mM stock solution in DMSO and subsequently diluted in culture medium for all experiments. The final concentration of DMSO was maintained at or below 0.1% throughout the study. Add 1/10 volume of CCK-8 reagent (Cell Counting Kit-8; GLPBIO, Montclair, CA, USA) to each well and place in the incubator (5% CO_2 and 37°C) for 2 h. Finally, BMECs' viability was measured at 450 nm by a microplate reader (Cytation5; Biotek, Winooski, VT, USA).

2.4. Malondialdehyde (MDA) and ROS Measurements

BMECs were inoculated into 6-well (3×10^5 cells per well) or 12-well plates (Cell slide; 1×10^5 cells per well), and MDA content and ROS levels in BMECs were detected using the MDA assay kit (Solarbio, Beijing, China) and DCFH-DA (Dichlorofluorescin diacetate) probe (Solarbio) after OGD/R or riluzole treatment following the manufacturer's instruction.

2.5. Transcriptome sequencing

HBMECs were seeded into culture dishes, and OGD/R treatment was initiated when cell confluence reached 70%-80%. The cells were subjected to 2 h of OGD followed by 24 h of reoxygenation. Total RNA was then extracted from both treated and control cells for RNA sequencing analysis, with three biological replicates included per group. Briefly, TriQuick Reagent (Solarbio) was added for cell lysis. The lysates were then submitted to Novogene (Beijing, China) for transcriptome sequencing analysis. The transcriptome sequencing libraries were constructed using the Fast RNA-seq Lib Prep Kit V2 (ABclonal, Wuhan, Hubei, China) according to the manufacturer's instructions. The final qualified libraries were sequenced on an Illumina Novaseq platform, yielding approximately 6 GB of raw data per sample. Genes significantly differentially expressed between Control and OGD/R groups were screened using edgeR software according to the criteria of $|\log_2(\text{Fold Change})| \geq 1$ & FDR ≤ 0.05, with $P < 0.05$ being considered as a significant difference. Cluster Profiler software was used to analyze the GO function enrichment and KEGG pathway enrichment of the differential genes, and $P < 0.05$ was considered significant

to analyze the functions of the differential genes and the signaling pathways involved between the Control group and the OGD/R group.

2.6. Immunofluorescence

1×10^5 hBMECs were seeded on the cell slide in each well of the 12-well plate in advance. After the cells adhered to the wall, they were washed with PBS (Biosharp) and then fixed with 4% paraformaldehyde (Biosharp). The cells were permeabilized using 0.5% Triton solution (BioFroxx, Einhausen, Germany) for 10 min, blocked with 2% BSA (Sangon Biotech, Shanghai, China) for 2 h, and then primary antibodies (CD31/PECAM1 Rabbit mAb (1:200); ABclonal) diluted with 2% BSA were added and incubated overnight at 4°C. At the end of primary antibody incubation, secondary antibody (ABflo™ 488-conjugated Goat Anti-Rabbit IgG (H+L) (1:500); ABclonal) diluted with 2% BSA was added and incubated at room temperature for 2 h. Subsequently, the nuclei were stained with DAPI (1:2000; Solarbio) for 10 min, and then the slices were photographed using a confocal microscope (Revolution WD, Andor, South Windsor, CT, USA).

2.7. Construction of stable cell lines

The pLVX-Puro-SLC7A11 overexpression plasmid and the pGreen-Puro-SLC7A11 knockdown plasmid were constructed using homologous recombination and T4 ligation, respectively. The specific PCR primers used for plasmid construction are listed in **Table S1**. Constructing hBMEC SLC7A11 overexpressing and knocking down stable transgenic cell lines using lentiviral infection. Briefly, use Lipofectamine™ 3000 (Invitrogen, Carlsbad, CA, USA) to transfect the plasmid (Gag-Pol: Vsvg: pLVX-Puro-SLC7A11 = 3:1:1) into 293T cells for lentivirus amplification. Viruses were collected at 72 h post-transfection. After passing through 0.45-μm filters, and then using the filtered virus solution to infect hBMEC. Cells were transduced with lentivirus at a multiplicity of infection (MOI) of 10, using viral particles with a titer of 1×10^8 TU/mL. After 72 h of virus infection, 2 μg/mL puro was used for screening, followed by quantitative reverse transcription polymerase chain reaction (RT-qPCR) and Western Blot (WB) verification.

2.8. Cell migration analysis

For cell migration analysis, scratch tests and transwell assays were performed. For the scratch test, a scratch was made after OGD/R, and the extent of cell migration was measured after 0 and 24 h. The transwell assay was also conducted after OGD/R. A total of 2×10^4 BMECs (serum-free culture medium) were cultured in the upper chamber, and the complete medium was added to the

lower chamber. After 24 h, cells in the lower chamber were fixed with 4% paraformaldehyde and stained with crystal violet. The extent of cell migration was determined by observing the cells in the lower chamber under a microscope.

2.9. Tube formation

BMECs were inoculated into 6-well plates (3×10^5 cells per well) for OGD/R or riluzole treatment. Subsequently, each group of cells was digested using trypsin and resuspended in serum-free culture medium. The digested cells were seeded into a 96-well plate (2×10^4 cells per well) covered with Matrigel (50 μL/well) and placed in a 37°C, 5% CO_2 incubator for 6 h. Subsequently, the degree of cell tube formation was observed under a microscope.

2.10. Permeability test

Transwell cell culture plates (24-well, 0.4 μm pore size, 6.5 mm diameter; LABSELECT, Hefei, Anhui, China) were used for the permeability test. BMECs were inoculated in transwell chambers (2×10^4 cells per well) and incubated at 37°C in a 5% CO_2 incubator. The cells were cultured until they were fully integrated and then treated with OGD/R and riluzole. To assess paracellular permeability, 20 μg/mL FITC-dextran (70 kDa; Sigma-Aldrich) was added to the upper chamber for 1 h after treatment. After incubation for 1 h, 100 μL of medium was collected from the abluminal chamber and added to a black 96-well plate. Fluorescence intensity was measured using a microplate reader (492/518 nm; Biotek).

2.11. Middle cerebral artery occlusion/reperfusion (MCAO/R)

Male C57BL/6 mouse (7-8 weeks old, 23-24 g) underwent MCAO/R modeling. Mouse was anesthetized with 2% isoflurane for induction and maintained under 1.5% isoflurane. Positioned supine with neck hair removed, a left-of-midline incision exposed the common carotid artery (CCA), which was clamped, and the vagus nerve dissected. The external carotid artery (ECA) and internal carotid artery (ICA) were isolated; the ECA was ligated. A monofilament was inserted via an incision below the ECA ligation to the clamp, then directed into the ICA and advanced ~8-9 mm into the middle cerebral artery (MCA) until resistance was met. The incision was sutured, and mouse were kept at 28°C. After 1 h ischemia, the filament was withdrawn for reperfusion. The entry site was ligated, the wound closed, and the mouse returned to housing upon recovery. For treatment, therapeutic agents were intraperitoneally administered at reperfusion onset.

2.12. TTC staining

Mouse was anesthetized using 1% sodium pentobarbital administered intraperitoneally at a dosage of 50 mg/kg body weight. Following complete anesthesia, the mouse was decapitated, and their brains were rapidly removed and placed on ice. The isolated brains were then positioned in a brain matrix and serially sectioned coronally into five 2-mm-thick slices. The brain sections were immersed in 1% 2,3,5-triphenyltetrazolium chloride (TTC) solution and incubated at 37℃ in the dark for 20 minutes; during incubation, the sections were covered with coverslips to prevent floating and ensure even staining. After complete staining, the TTC solution was replaced with 4% paraformaldehyde for post-fixation, and the sections were stored at 4℃ overnight. Finally, images of the stained brain sections were captured the following day.

In this study, animals were randomized into four groups: sham-operated group, model group, and riluzole treatment groups (2, 4, 8, and 12 mg/kg), with 3 mice per group. The randomization procedure was as follows: all eligible mice was assigned unique identification numbers, and a computer-generated random number sequence was used to allocate them to the different groups. Throughout the drug administration and behavioral assessments, the experimenters were blinded to the group assignments. No animal mortality occurred during the entire experimental period. Predefined exclusion criteria included: 1) surgical error, 2) presence of predefined severe neurological deficits or compromised health status within 24 h after surgery, and 3) death before tissue collection due to non-model-related causes.

2.13. Evans blue staining

Blood-brain barrier integrity was assessed by Evans Blue (EB) extravasation. Mouse received a 2% EB solution in PBS (4 mL/kg) via tail vein injection, allowing circulation for 2 h. Following transcardial perfusion with PBS, brains were removed for photographic documentation. The lesioned hemisphere was weighed, homogenized in PBS, and centrifuged (13,000 rpm, 30 min, 4℃). The supernatant was mixed with an equal volume of trichloroacetic acid and reacted overnight at 4℃. After further centrifugation (13,000 rpm, 30 min, 4℃), the final supernatant's absorbance at 620 nm was measured using a microplate reader. In this study, animals were randomized into three groups: sham-operated group, model group, and riluzole-treated group, with 3 mice in each group. The randomization procedure and exclusion criteria were identical to those described above. All animals survived the entire experimental period, with no mortality observed.

2.14. Neurological impairment score

Neurological deficits were assessed 24 h post-reperfusion in MCAO-modeled mice using a composite scoring system (0-14 points). After 2 h of dark adaptation, blinded evaluators tested the mouse in four domains: 1) Tail suspension: scoring forelimb flexion, hindlimb flexion, and head deviation (max 3 points); 2) Open field walking: scoring gait abnormalities and circling (0-3 points); 3) Beam balance test (1.5 cm width): scoring balance ability and falls (0-6 points); and 4) Reflex absence: scoring pinna and corneal reflexes (0-2 points). Scores reflected motor coordination, balance, and reflex function. In this study, animals were completely randomized into three groups: sham-operated group, model group, and riluzole-treated group, with 5 mice in each group. The randomization procedure and exclusion criteria were identical to those described above. All animals survived the entire experimental period, with no mortality observed.

2.15. RNA extraction and RT-qPCR

Total RNA was extracted from BMECs using TriQuick Reagent (Solarbio) and subjected to reverse transcription (Vazyme, Nanjing, Jiangsu, China). cDNA amplification was carried out using M5 Hiper SYBR Premix EsTaq (Mei5bio, Beijing, China) on a CFX96 Touch (Bio-Rad, Hercules, CA, USA). The cDNA was denatured by 40 PCR cycles (95°C, 30 s; 95°C, 5 s; 60°C, 30 s). The RT-qPCR primers were designed and synthesized by Tsingke Biotech (Beijing, China), and the sequences are listed in **Table S1**. *β-actin* was the invariant control, and the relative level of mRNA was calculated using the $2^{-\Delta\Delta Ct}$ method.

2.16. Western blot

BMECs protein was collected rapidly by scraping with ice-cold RIPA lysis buffer containing the Phenylmethylsulfonyl fluoride (PMSF; Biosharp). The protein concentration was determined using the BCA Protein Concentration Assay Kit (Biosharp). An equal amount of cell lysates was separated with 10% SDS-PAGE gel and then subsequently transferred to a Polyvinylidene difluoride (PVDF) membrane (Sigma-Aldrich). These membranes were blocked with 5% nonfat dried milk for 2 h and incubated with the following primary antibodies: Beta Actin Monoclonal antibody (1:5000; Proteintech, Wuhan, Hubei, China), ZO-1 (D6L1E) Rabbit mAb (1:1000; Cell Signaling Technology, Boston, MA, USA), Claudin 5 Polyclonal Antibody (1:2500; Thermo Fisher, Waltham, MA, USA), Occludin Polyclonal antibody (1:5000; Proteintech), SLC7A11/xCT Rabbit mAb (1:2500; ABclonal), GPX4 Rabbit mAb (1:1000; ABclonal), Anti-HIF-1 alpha antibody (1:1000,

Abcam, Cambridge, MA, USA), VEGFA Polyclonal antibody (1:1000; Proteintech) and PHD2/EGLN1 Polyclonal antibody (1:5000; Proteintech) at 4°C overnight. β-actin was used as a loading control. Next day, the PVDFs were washed and incubated with secondary antibodies (HRP Goat Anti-Rabbit IgG (H+L) (1:5000; ABclonal) and HRP-conjugated Affinipure Goat Anti-Mouse IgG (H+L) (1:5000; Proteintech)) for 1.5 h at room temperature. The ECL chemiluminescence substrate kit (Biosharp) is used to visualize protein bands on the chemiluminescence gel imaging system (ChemiDoc XRS+; Bio-Rad).

2.17. Statistical analysis

All data were analyzed by SPSS 26.0 and presented as mean ± SEM of three independent experiments. GraphPad Prism 9.0 was used to plot gene expression profiles. Statistical significance was determined by one-way ANOVA, followed by Tukey's post-hoc test for multiple comparisons. One asterisk and two asterisks indicated $P < 0.05$ and $P < 0.01$ between groups, respectively.

3. Results

3.1. Transcriptomic profiling of hBMEC following OGD/R treatment

Transcriptomic analysis revealed a total of 151 significantly different genes (DEGs) in the OGD/R group compared to the control, with 60 genes significantly upregulated and 91 downregulated **(Fig. 1A-C)**. To validate the RNA-seq results representative DEGs were randomly selected for RT-qPCR. The expression trends of upregulated genes (*GPM6A*, *ESRRB*, *SLC2A4*, *FGFBP1*) and downregulated genes (*SLC7A11*, *SPOCD1*, *TLN2*, *NLRP1*, *ISLR*, *AQP1*, *BCAT1*) were consistent with the sequencing data, confirming the reliability of the transcriptomic analysis. **(Fig. 1D)**.

Gene Ontology (GO) functional enrichment analysis identified the top 10 most significantly enriched terms across Biological Process (BP), Cell Component (CC), and Molecular Function (MF) categories, visualized via bubble charts **(Fig. 1E)**. Enriched BP terms were predominantly associated with cellular and aerobic respiration, oxidative phosphorylation, the respiratory electron transport chain, and ATP synthesis coupled to electron transport. CC terms mainly involved the mitochondrial inner membrane, ribosomes and their subunits, and mitochondrial protein complexes. MF enrichment included molecular transducer and signaling receptor activity, the structural constituent of ribosomes, and oxidoreduction-driven active transmembrane transporter activity. These findings indicate significant changes in transmembrane transport and aerobic metabolism in

hBMECs following OGD/R.

KEGG pathway enrichment analysis further revealed significant involvement of neurological diseases, including Parkinson's disease, Huntington's disease, prion disease, amyotrophic lateral sclerosis, and ribosome-associated pathways, aligning with previous findings that implicate vascular endothelial involvement in neurological dysfunction under ischemic stress **(Fig. 1F)**.

Focusing on membrane-associated targets, we prioritized membrane-localized DEGs using literature and LocTree3 predictions. From this refined pool, SLC7A11 was selected based on: significant differential expression, confirmed plasma membrane localization as the cystine/glutamate antiporter (system xc-), and its critical, established role in regulating redox homeostasis (via glutathione synthesis) and inhibiting ferroptosis. Crucially, ferroptosis and oxidative stress are key drivers of endothelial dysfunction in ischemic-reperfusion injury (IRI). Among these, SLC7A11, a membrane-localized protein, was selected for further mechanistic investigation due to its potential relevance in the endothelial response to ischemic-reperfusion injury.

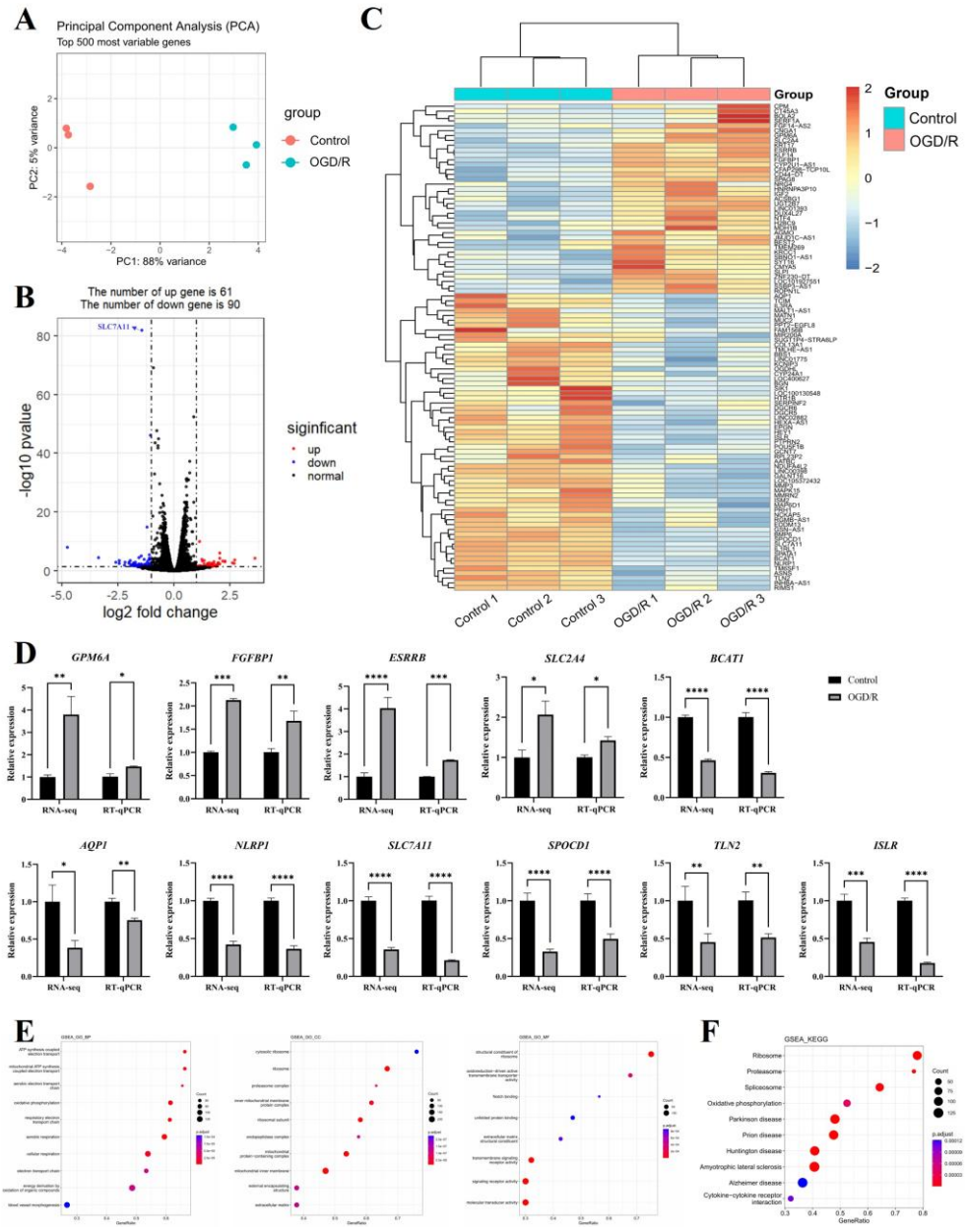

Fig. 1 Transcriptomic analysis of hBMECs after OGD/R. (A) Principal component analysis (PCA) of transcriptome data from control and OGD/R-treated hBMECs, $n = 3$ biological replicates. **(B)** Volcano plot of differentially expressed genes (DEGs) (threshold: $|\log_2 FC| \geq 1$, FDR-adjusted $p \leq 0.05$), highlighting 60 upregulated (red) and 91 downregulated (blue) transcripts. SLC7A11 is annotated. (**C)** Hierarchical clustering heatmap of DEGs across biological replicates. (**D)** RT-qPCR validation of 11 representative DEGs. $n = 3$ biological replicates. Statistical significance was determined by one way ANOVA followed by Tukey's post-hoc test: $^{*}P < 0.05$, $^{**}P < 0.01$, $^{***}P < 0.001$, $^{****}P < 0.0001$. **(E)** GO enrichment analysis of DEGs. **(F)** KEGG pathway analysis of DEGs.

3.2. SLC7A11 overexpression attenuates OGD/R-induced oxidative stress in hBMECs

To directly confirm ferroptosis in our OGD/R model, we applied Ferrostatin-1 (Fer-1), a specific ferroptosis inhibitor. Treating cells with increasing concentrations of Fer-1 (0–10 μM) during OGD/R resulted in a marked, dose-dependent improvement in cell viability **(Fig. S4A)**. Furthermore, at the molecular level, Fer-1 (10 μM) significantly suppressed the OGD/R-induced upregulation of *ACSL4* mRNA **(Fig. S4B)**, a pivotal positive regulator of ferroptosis. These results demonstrate that ferroptosis significantly contributes to OGD/R-induced cell injury.

To further corroborate this finding through a genetic approach, we successfully constructed the pLVX-Puro-SLC7A11 overexpression plasmid through homologous recombination **(Fig. S5)**, and established stable overexpression cell lines using lentiviral transduction. As shown in **Fig. 2A and B**, both mRNA and protein levels of SLC7A11 were notably upregulated in the OE-SLC7A11 group compared to the OE-NC group, confirming the successful generation of hBMECs with stable SLC7A11 overexpression.

Following OGD/R treatment, overexpression of SLC7A11 significantly increased cell viability and mitigated OGD/R-induced cytotoxicity **(Fig. 2C)**. Biochemical assays further revealed that SLC7A11 overexpression markedly reduced intracellular MDA and ROS levels, indicating a substantial alleviation of oxidative stress **(Fig. 2D-F)**.

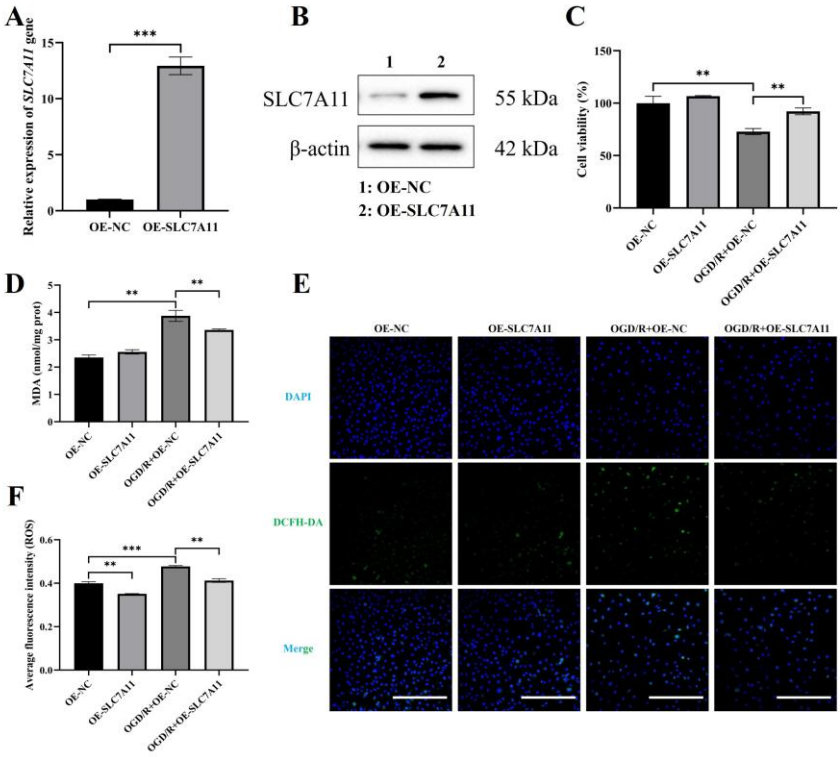

Fig. 2 SLC7A11 overexpression attenuate oxidative damage produced by OGD/R in hBMECs. **(A)** RT-qPCR analysis of *SCL7A11* mRNA expression in OE-NC and OE-SLC7A11 groups. **(B)** Western blot quantification of SCL7A11 protein levels in OE-NC and OE-SLC7A11 groups. **(C)** Cell activity assessed by CCK-8 assay under OGD/R conditions. **(D)** MDA content measurement reflecting lipid peroxidation levels. **(E)** Representative images of intracellular ROS detection using DCFH-DA fluorescent probe. **(F)** Quantification and statistical analysis on DCFH-DA fluorescence intensity in different groups. Data are presented as mean ± SEM (n = 3 biological replicates). Statistical significance was determined by one way ANOVA followed by Tukey's post-hoc test: $^{**}P < 0.01$, $^{***}P < 0.001$. Scale bar = 100 μm.

3.3. SLC7A11 overexpression rescues hBMEC migration, barrier integrity, and angiogenic capacity post-OGD/R

We next assessed the impact of SLC7A11 overexpression on cellular functions post-OGD/R. Migration assays, permeability tests, and tube formation assays demonstrated that OGD/R significantly impaired hBMEC motility **(Fig. 3A–D)**, barrier integrity **(Fig. 3E)**, and angiogenic potential **(Fig. 3J–K)**. Notably, these impairments were substantially reversed in the OE-SLC7A11 group. Furthermore, tight junction proteins at both the mRNA and protein levels, which were significantly reduced following OGD/R, were restored upon SLC7A11 overexpression **(Fig. 3F–I)**, corroborating the permeability assay results.

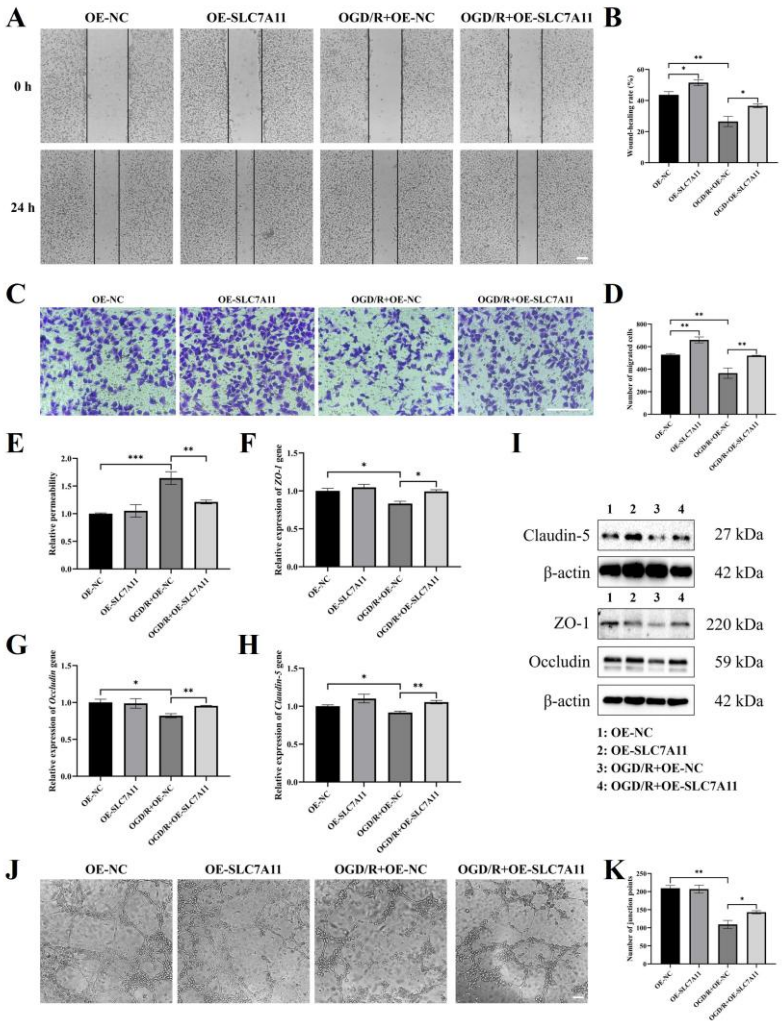

Fig. 3 SLC7A11 overexpression mitigates OGD/R-induced impairments in hBMEC migration, integrity, and tube formation capacity. (A) Representative image of scratch wound healing assay. **(B)** Quantification of cell migration recovery area at 24 h post-scratch. **(C)** Representative images of transwell migration assay. **(D)** Quantitative analysis of migrated cells per field. **(E)** Endothelial barrier permeability assessed by FITC-dextran flux. **(F-H)** mRNA expression levels of tight junction markers: **(F)** *ZO-1*, **(G)** *Occludin*, **(H)** *Claudin-5* via RT-qPCR. **(I)** Western blot analysis of tight junction proteins expression. **(J)** Representative images of tube formation assay on Matrigel. **(K)** Quantification of vascular network junctions. Data expressed as mean ± SEM (n = 3 biological replicates). Statistical significance determined by one way ANOVA followed by Tukey's post-hoc test: *$P < 0.05$, **$P < 0.01$, ***$P < 0.001$. Scale bar (A, C, J) = 100 μm.

3.4. SLC7A11 overexpression regulates GPX-4 and HIF-1α/VEGFA to alleviates hBMEC injury

Previous studies have demonstrated that the SLC7A11/GPX-4 pathway plays a crucial role in the process of ferroptosis. Therefore, we investigated whether SLC7A11 overexpression mitigated

the damage caused by OGD/R to hBMECs by enhancing the expression of GPX-4. Our findings revealed that the overexpression of SLC7A11 robustly upregulated GPX-4 expression, both under basal conditions and following OGD/R, thereby suggesting a protective effect through ferroptosis suppression **(Fig. 4A-C)**. Additionally, because the HIF-1α/VEGFA pathway is well known to regulate angiogenesis, we investigated whether it also contributes to the effects of SLC7A11 overexpression. The results revealed that SLC7A11 overexpression promoted HIF-1α and VEGFA expression **(Fig. 4D)**, and this upregulation persisted after OGD/R treatment, suggesting a role in promoting angiogenic and reparative processes via the HIF-1α/VEGFA pathway.

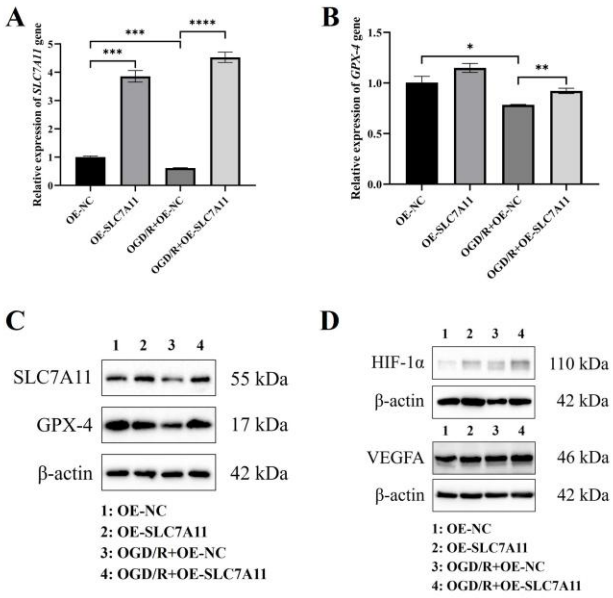

Fig. 4 SLC7A11 overexpression upregulates GPX-4 and HIF-1α/VEGFA expression, thereby alleviating hBMEC injury. (A) *SLC7A11* and **(B)** *GPX-4* mRNA expression analysis by RT-qPCR. **(C)** Western blot analysis of SLC7A11 and GPX4 protein expression, and **(D)** HIF-1α and VEGFA protein expression Data presented as mean ± SEM (n = 3 biological replicates). Statistical significance was determined by one way ANOVA followed by Tukey's post-hoc test: *$P < 0.05$, **$P < 0.01$, ***$P < 0.001$, ****$P < 0.0001$.

3.5. Riluzole promotes SLC7A11 expression and attenuates OGD/R-induced oxidative stress in BMECs

Through analysis on the cMAP online website (https://clue.io/) and a comprehensive literature review, it was discovered that riluzole serves as an activator of *SLC7A11* gene expression **[19]**. Experimental results obtained by introducing riluzole to hBMEC culture demonstrated an up-regulation of SLC7A11 expression at both mRNA and protein levels, thereby providing further

evidence supporting the claim that riluzole acts as an activator of SLC7A11 expression **(Fig. 5A and B)**.

The riluzole powder was dissolved in DMSO to a concentration of 10 mM and then sequentially diluted to concentrations of 2.5 μM, 5 μM, 10 μM, 20 μM, 40 μM, 80 μM, and 160 μM. During reoxygenation of OGD/R for treatment, the corresponding concentration of riluzole was added. The results indicated that as the concentration increased, the cellular activities of hBMEC and BEND3 initially increased and then decreased. This suggests that riluzole could alleviate the decrease in cellular activity caused by OGD/R on BMECs. To further determine whether the protective effect of riluzole depends on SLC7A11, we generated an SLC7A11-knockdown hBMEC cell line. Under OGD/R conditions, SLC7A11 knockdown markedly decreased cell viability, and this reduction was not rescued by riluzole treatment **(Fig. S6)**. These results indicate that the protective effect of riluzole against OGD/R-induced injury in hBMECs is dependent on SLC7A11. Inflection points were observed at concentrations of 5 μM and 2.5 μM for hBMEC **(Fig. 5C)** and BEND3 **(Fig. S7A)**, respectively. In further experiments, we treated hBMEC and BEND3 cells with riluzole at concentrations of 5 μM and 2.5 μM, respectively. Our findings indicate that riluzole effectively mitigated the oxidative damage induced by OGD/R in hBMEC **(Fig. 5D-F)** and BEND3 **(Fig. S7B-D)**.

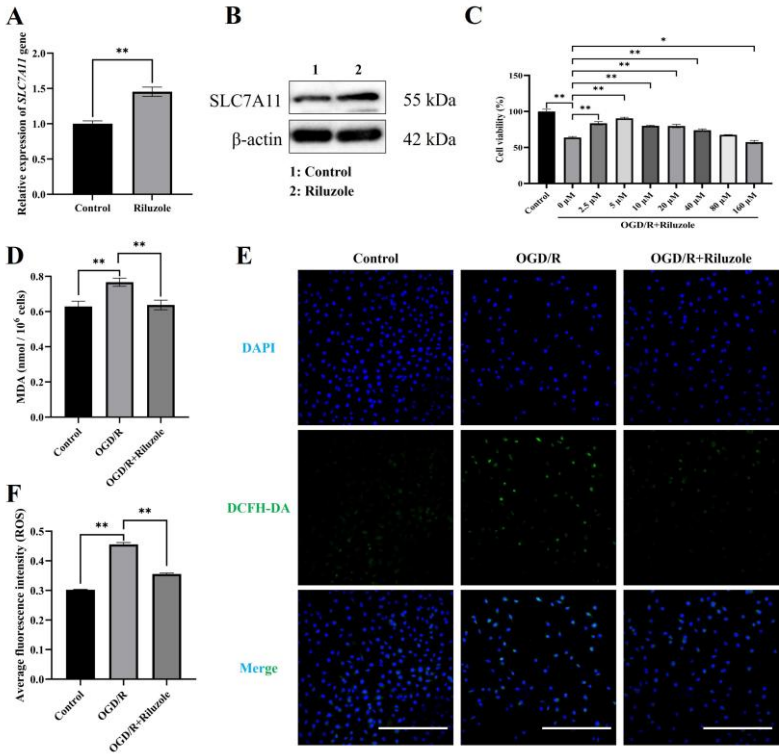

Fig. 5 Riluzole promotes SLC7A11 expression and attenuates OGD/R-induced oxidative damage in hBMECs. (A) Riluzole treatment upregulates SLC7A11 mRNA expression. **(B)** Riluzole treatment upregulates SLC7A11 protein level. **(C)** Dose-dependent effects of riluzole on hBMEC viability assessed by CCK-8 assay. **(D)** Effect of riluzole treatment on MDA content of hBMECs after OGD/R. **(E)** Representative images of intracellular ROS detection using DCFH-DA fluorescent probe. **(F)** Quantification and statistical analysis on DCFH-DA fluorescence intensity in different groups. Data expressed as mean ± SEM ($n = 3$ biological replicates). Statistical significance determined by one way ANOVA followed by Tukey's post-hoc test: $^{*}P < 0.05$, $^{**}P < 0.01$. Scale bar = 100 μm.

3.6. Riluzole mitigates the effects of OGD/R on BMECs migration, integrity, and tube formation capacity

The effects of OGD/R on the migration, permeability, and tube formation ability of BMECs were investigated in Fig. 6. The results demonstrated that OGD/R significantly inhibited multiple functions of brain microvascular endothelial cells (BMECs). Specifically, in hBMEC cells, we observed a significant inhibition of migration **(Fig. 6A-C)**, a reduction in permeability **(Fig. 6D)**, and impaired tube formation ability **(Fig. 6I, J)**. Similarly, parallel experiments in BEND3 cells confirmed the significant inhibition of migration **(Fig. S8A-C)**, permeability **(Fig. S8D)**, and tube formation **(Fig. S8I, J)**. However, these effects were significantly relieved after riluzole treatment. Additionally, the mRNA and protein levels of tight junction proteins in BMECs were found to be significantly downregulated after OGD/R, but were relieved after riluzole treatment. These findings aligned with the outcomes of the in vitro permeability assay, which demonstrated a consistent phenotype in both hBMEC **(Fig. 6E-H)** and the corresponding BEND3 cell models **(Fig. S8E-H)**.

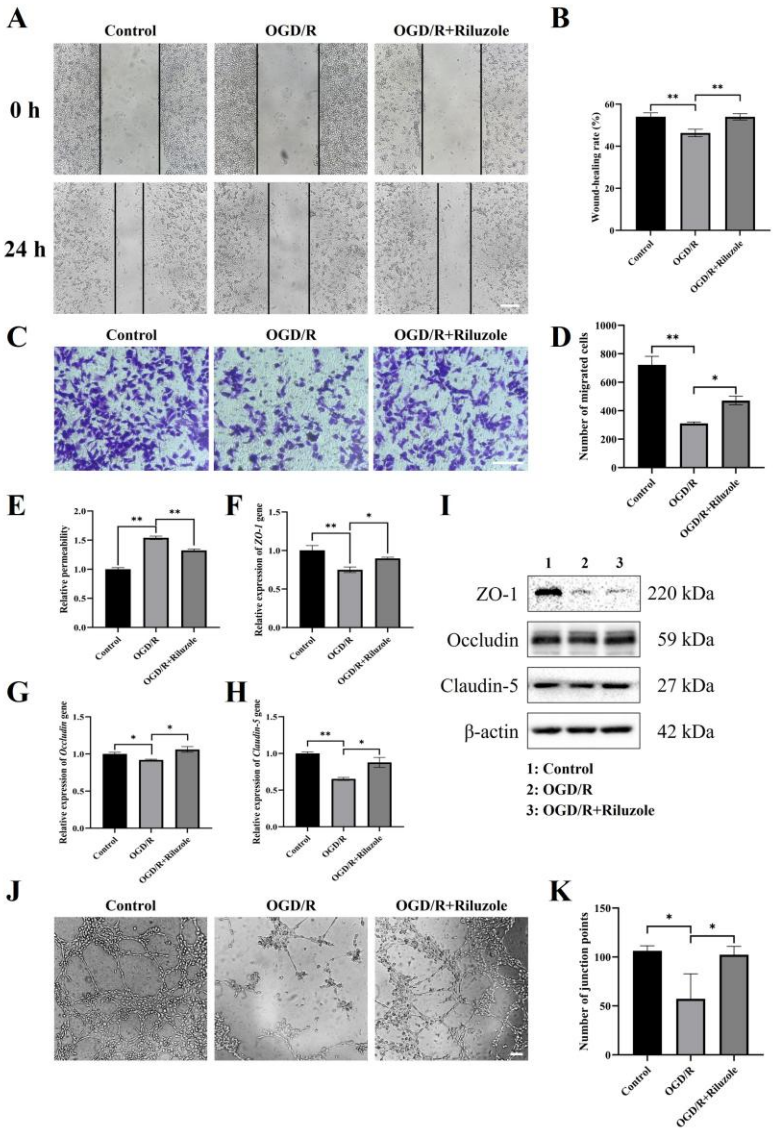

Fig.6 Riluzole attenuates OGD/R-induced impairments in hBMEC migration, integrity, and tube formation capacity. (A) Representative image of the scratch assay. **(B)** Quantification of cell migration recovery area. **(C)** Representative images of transwell migration assay detection of cell migration ability. **(D)** Quantitative analysis of migrated cells per field. **(E)** Endothelial barrier permeability assessed by FITC-dextran flux. **(F-H)** Effects of riluzole treatment on mRNA expression levels of tight junction markers: **(F)** *ZO-1*, **(G)** *Occludin*, **(H)** *Claudin-5* via RT-qPCR. **(I)** Effect of riluzole treatment on hBMEC tight junction protein level after OGD/R. **(J)** Representative images of tube formation assay on Matrigel. **(K)** Quantification of vascular network junctions. Data expressed as mean ± SEM (n = 3 biological replicates). Statistical significance determined by one way ANOVA followed by Tukey's post-hoc test: *P < 0.05, **P < 0.01. Scale bar (A, C, J) = 100 μm.

3.7. Riluzole mitigates OGD/R-induced damage to BMECs by modulating the SLC7A11/GPX-4 and SLC7A11/HIF-1α/VEGFA pathways

Riluzole will activate the expression of SLC7A11, and the elevated expression of SLC7A11 will alleviate the damage of OGD/R to hBMEC by regulating GPX-4 and HIF-1α/VEGFA pathways. Therefore, we hypothesize that riluzole may also alleviate the damage caused by OGD/R to BMECs by regulating SLC7A11/GPX-4 and SLC7A11/HIF-1α/VEGFA pathways. Our results showed that in hBMEC cells, the mRNA and protein levels of SLC7A11 and GPX-4 were downregulated after OGD/R, which was restored by riluzole treatment **(Fig. 7A-C)**. A similar pattern was observed in BEND3 cells, where riluzole reversed the OGD/R-induced decreases in SLC7A11 and GPX-4 expression **(Fig. S9A-C)**. We further investigated the effect of riluzole on the SLC7A11/HIF-1α/VEGFA pathway and found that the expression levels of HIF-1α and VEGFA were upregulated after OGD/R in both hBMEC and BEND3 cells, which is consistent with previous studies **[20**,**21]**. Notably, riluzole did not reverse this effect, with both factors remaining elevated in hBMEC **(Fig. 7D)** and BEND3 cells **(Fig. S9D)**. These results suggest that riluzole may regulate the SLC7A11/GPX-4 and SLC7A11/HIF-1α/VEGFA pathways, thereby alleviating the damage caused by OGD/R to BMECs.

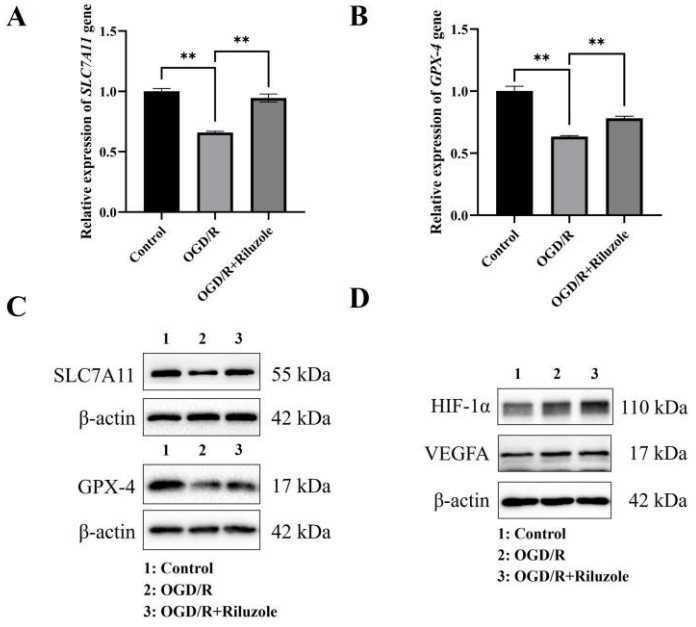

Fig. 7 Riluzole mitigates OGD/R-induced damage in hBMEC by dually modulating the SLC7A11/GPX-4 and SLC7A11/HIF-1α/VEGFA pathways. (A) Effect of riluzole treatment on *SLC7A11* mRNA expression in hBMEC after OGD/R. **(B)** Effect of riluzole treatment on *GPX-4*

mRNA expression in hBMEC after OGD/R. **(C)** Effect of riluzole treatment on SLC7A11 and GPX-4 protein expression in hBMEC after OGD/R. **(D)** Effect of riluzole treatment onHIF-1α and VEGFA protein expression in hBMEC after OGD/R. Data expressed as mean ± SEM (n = 3 biological replicates). Statistical significance determined by one way ANOVA followed by Tukey's post-hoc test: $^{**}P < 0.01$.

3.8. Riluzole alleviates neurological injury by reducing blood-brain barrier permeability in MCAO/R mouse

To evaluate the neurovascular protective effects of riluzole following cerebral ischemia-reperfusion, we employed the MCAO/R model in mice. Riluzole was administered intraperitoneally at doses of 2, 4, 8, or 12 mg/kg immediately upon reperfusion. TTC staining performed 24 h after reperfusion demonstrated a dose-dependent response: infarct area was reduced at 2 and 4 mg/kg but increased at higher doses (8 and 12 mg/kg), suggesting a narrow therapeutic window. The most significant neuroprotection was observed at 4 mg/kg, which was subsequently selected for downstream experiments **(Fig. S10)**.

At 24 h post-reperfusion, 4 mg/kg riluzole treatment significantly reduced Evans blue extravasation compared to the MCAO/R group, indicating improved BBB integrity **(Fig. 8A)**. Western blot analysis further revealed that riluzole restored the expression of tight junction proteins (ZO-1, Occludin, and Claudin-5), which were markedly decreased in the ischemic hemisphere following MCAO/R **(Fig. 8B)**, supporting its protective role on BBB structure.

qPCR analysis showed that ischemia-reperfusion injury induced a strong pro-inflammatory response, as evidenced by elevated mRNA levels of *IL-1β*, *IL-6*, *TNF-α*, *COX-2*, and *MCP-1*, alongside an increase in anti-inflammatory *IL-10*. Treatment with riluzole significantly suppressed the expression of these pro-inflammatory cytokines while further enhancing IL-10 levels, indicating its anti-inflammatory effect and modulation of the post-ischemic immune response **(Fig. 8C)**.

Behavioral assessments-including tail suspension test, spontaneous locomotion, beam walking, and neurological reflex scoring-revealed severe functional impairments in MCAO/R mouse, which were significantly ameliorated by riluzole administration **(Fig. 8D)**. These findings collectively demonstrate that riluzole confers neuroprotection by preserving BBB integrity, mitigating neuroinflammation, and improving functional recovery following ischemia-reperfusion injury.

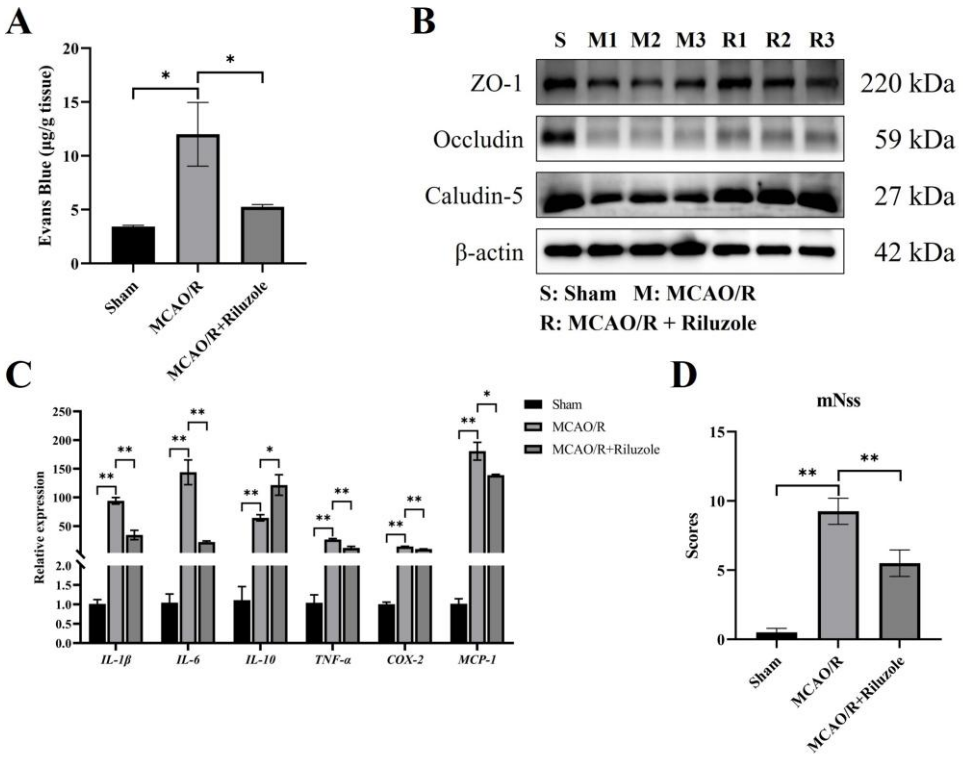

Fig. 8 Riluzole preserves blood-brain barrier integrity and improves neurological outcomes in MCAO/R mouse. (A) Quantification of Evans blue dye extravasation 24 h after MCAO/R. **(B)** Western blot analysis of tight junction proteins (ZO-1, Occludin, Claudin-5) in the ischemic hemisphere following riluzole treatment. **(C)** qPCR analysis of pro-inflammatory cytokines (*IL-1β*, *IL-6*, *TNF-α*, *COX-2*, *MCP-1*) and anti-inflammatory IL-10 in brain tissue. **(D)** Neurological function scores based on composite behavioral assessments following reperfusion. Data are presented as mean ± SEM (Data in panels (A)-(C) are representative of $n = 3$ biological replicates, while data in panel (D) are from $n = 5$ biological replicates). Statistical significance determined by one-way ANOVA followed by Tukey's post-hoc test: $^{**}P < 0.01$.

4. Discussion

Ischemic stroke is a devastating condition marked by the abrupt disruption of cerebral blood flow and subsequent reperfusion-induced injury, in which BBB breakdown plays a pivotal role in driving secondary neuronal damage and limiting recovery **[22-26]**. Brain microvascular endothelial cells (BMECs), the structural and functional backbone of the BBB, are particularly susceptible to oxidative and inflammatory stress during ischemia-reperfusion, making them an attractive yet underexplored target for therapeutic intervention **[27]**. In this study, we systematically dissected and functionally characterized the molecular perturbations in BMECs under OGD/R and identified

SLC7A11 as a critical regulator of endothelial integrity and survival. Importantly, we demonstrated that pharmacological activation of SLC7A11 by riluzole not only rescued BMEC function but also conferred neurovascular protection in a mouse model of stroke **(Fig. 9)**.

Through transcriptomic profiling of hBMECs subjected to OGD/R, we identified broad downregulation of genes involved in oxidative metabolism and redox homeostasis, with SLC7A11 emerging as a top candidate. SLC7A11 encodes xCT, the catalytic subunit of the cystine/glutamate antiporter, which mediates cystine uptake essential for glutathione (GSH) synthesis **[28-34]**. As a central gatekeeper of ferroptosis resistance, SLC7A11 maintains redox balance via the GSH-GPX4 axis, preventing accumulation of lipid peroxides. In our model, SLC7A11 expression was significantly suppressed following OGD/R, concomitant with increased oxidative stress and endothelial dysfunction **[35-37]**. Overexpression of SLC7A11 restored GSH-associated antioxidant capacity, reduced lipid peroxidation and ROS levels, and improved cell viability. These findings collectively suggest that OGD/R-induced endothelial injury is at least partially mediated through ferroptosis mechanisms.

Interestingly, our data revealed that SLC7A11 overexpression also enhanced the migratory, barrier-forming, and angiogenic capacities of hBMECs after OGD/R. This phenotype extended beyond redox regulation, implicating a broader, potentially indirect signaling role for SLC7A11 in vascular remodeling. Mechanistically, SLC7A11 overexpression was found to upregulate HIF-1α and its angiogenic target VEGFA, and this effect persisted under OGD/R conditions. This finding aligns with emerging evidence that metabolic rewiring via glutamate depletion and TCA cycle suppression stabilizes HIF-1α by inhibiting prolyl hydroxylase (PHD) activity, thereby promoting angiogenic signaling **[17,38-44]**. These results suggest that SLC7A11 may contribute to both ferroptosis resistance via GPX4 and, potentially, vascular repair pathways that involve HIF-1α/VEGFA signaling.

To assess the translational potential of targeting SLC7A11, we employed a computational drug-repurposing approach and identified riluzole, an FDA-approved ALS medication, as a putative SLC7A11 activator **[19,45,46]**. Experimental validation confirmed that riluzole treatment increased SLC7A11 expression in both human and mouse BMECs and restored redox balance under OGD/R. Functionally, riluzole rescued BMEC viability, reduced oxidative damage, restored tight junction protein expression, and promoted angiogenesis, closely phenocopied the effects of SLC7A11

overexpression. These effects were observed at physiologically relevant concentrations, suggesting clinical feasibility.

Importantly, riluzole's protective effects were validated *in vivo*. A dosage of 4 mg/kg was selected, as it has been consistently shown in prior studies to elicit significant biological activity **[47**,**48]**. This specific dosage is further supported by pharmacokinetic evidence demonstrating effective brain delivery and the attainment of therapeutically relevant concentrations in mice **[49]**. In the MCAO/R mouse model, riluzole administered immediately upon reperfusion significantly reduced cerebral infarct volume, attenuated BBB leakage (measured by Evans blue extravasation), and preserved tight junction integrity. Notably, riluzole also dampened neuroinflammatory responses, suppressing pro-inflammatory cytokines (IL-1β, IL-6, TNF-α) while enhancing anti-inflammatory IL-10. Behavioral assessments confirmed improved neurological outcomes, thus strongly linking BBB protection to functional recovery. These *in vivo* findings reinforce the central role of BMEC preservation in neuroprotection and substantiate riluzole's therapeutic relevance.

An unexpected observation was the narrow therapeutic window of riluzole in our *in vivo* experiments: doses above the effective 4 mg/kg (i.e., 8 and 12 mg/kg) paradoxically exacerbated infarct outcomes. Although the precise mechanism remains to be fully defined, several pharmacologically plausible explanations warrant consideration. First, supratherapeutic dosing may alter the balance of riluzole’s pharmacodynamic actions, allowing off-target effects—such as excessive inhibition of voltage-gated sodium channels or other ion conductances—to dominate and impair neurovascular homeostasis. Second, high-dose exposure may disrupt the SLC7A11–GPX4 axis, which is essential for riluzole’s protective efficacy; overwhelming this pathway could exacerbate oxidative or metabolic stress rather than alleviate it. Third, elevated systemic or brain concentrations might induce vascular or metabolic toxicity, leading to impaired perfusion or accentuated inflammatory responses. Together, these hypotheses underscore that future work integrating pharmacokinetic and dose-stratified pharmacodynamic analyses is needed to delineate the mechanistic basis of this inverted dose–response relationship.

An intriguing observation from our study is that SLC7A11 overexpression preserved endothelial cell viability even under GPX4 inhibition by RSL3, suggesting that SLC7A11 may exert GPX4-independent protective effects. One possible explanation involves metabolic regulation through glutamate efflux. Reduced intracellular glutamate levels may influence TCA cycle flux and

α-ketoglutarate availability, with downstream effects on HIF stabilization, as previously noted. Furthermore, SLC7A11 has also been implicated in other cell death pathways such as disulfidptosis **[50]**, warranting further investigation in the context of endothelial injury. Together, these findings highlight the multifaceted protective roles of SLC7A11 in cellular stress responses and suggest that its modulation could confer benefits extending beyond ferroptosis inhibition.

The present study has several implications. First, it identifies SLC7A11 as a nodal regulator at the intersection of oxidative stress, angiogenesis, and metabolic signaling in BMECs. Second, it provides compelling preclinical evidence that riluzole—a clinically available drug—can activate SLC7A11 and restore BBB function in stroke models. Third, it supports the concept of targeting endothelial health, rather than solely focusing on neurons, as a viable neuroprotective strategy in ischemic stroke.

Nevertheless, several questions remain open. The specific transcriptional and epigenetic mechanisms by which riluzole induces SLC7A11 remain undefined. While riluzole has been shown to inhibit glutamate release and modulate ion channels, the link to SLC7A11 gene expression requires further delineation. Additionally, the interaction of SLC7A11 with other ferroptosis regulators such as ACSL4, FSP1, or NRF2 in BMECs under ischemic stress remains to be clarified **[51-53]**. Future work should also assess the long-term effects of riluzole on BBB integrity and functional recovery in chronic stroke models and explore its synergistic potential with reperfusion therapies such as tPA or mechanical thrombectomy. Although the animal group sizes used in this study are appropriate for mechanistic interrogation, future studies employing larger cohorts will be necessary to further enhance statistical power and to validate the generalizability of these findings.

This study also found that SLC7A11 overexpression upregulates HIF-1α/VEGFA. To elucidate the mechanism, we examined PHD2 expression, a key negative regulator of HIF-1α **(Fig. S11)**. Notably, SLC7A11 overexpression did not alter the total protein level of PHD2, suggesting a regulatory mode independent of protein abundance. Given the central role of SLC7A11 in cystine uptake and cellular metabolism, we propose a novel possibility: SLC7A11 overexpression may create a microenvironment that inhibits PHD2 enzyme activity by altering intracellular metabolites (for example, reducing the α-ketoglutarate/succinate ratio) or diminishing ROS generation. This functional inhibition of enzyme activity, rather than regulation of protein expression, could be the key event leading to HIF-1α stabilization and the subsequent activation of the VEGFA pathway.

Therefore, the upregulation of HIF-1α/VEGFA by SLC7A11 is likely an indirect, context-dependent consequence of its primary role in regulating cellular redox and metabolic states.

In conclusion, this study elucidates a previously unrecognized role of SLC7A11 in maintaining BBB function during ischemic stress and identifies riluzole as an effective pharmacological activator of the SLC7A11/GPX4 and potential activator of the SLC7A11/HIF-1α/VEGFA pathways. Through integrated *in vitro* and *in vivo* experiments, we demonstrate that riluzole restores endothelial homeostasis, mitigates oxidative and inflammatory injury, and improves neurological function after stroke. These findings pave the way for repositioning riluzole as a potential endothelial-targeted therapy for ischemic cerebrovascular disease.

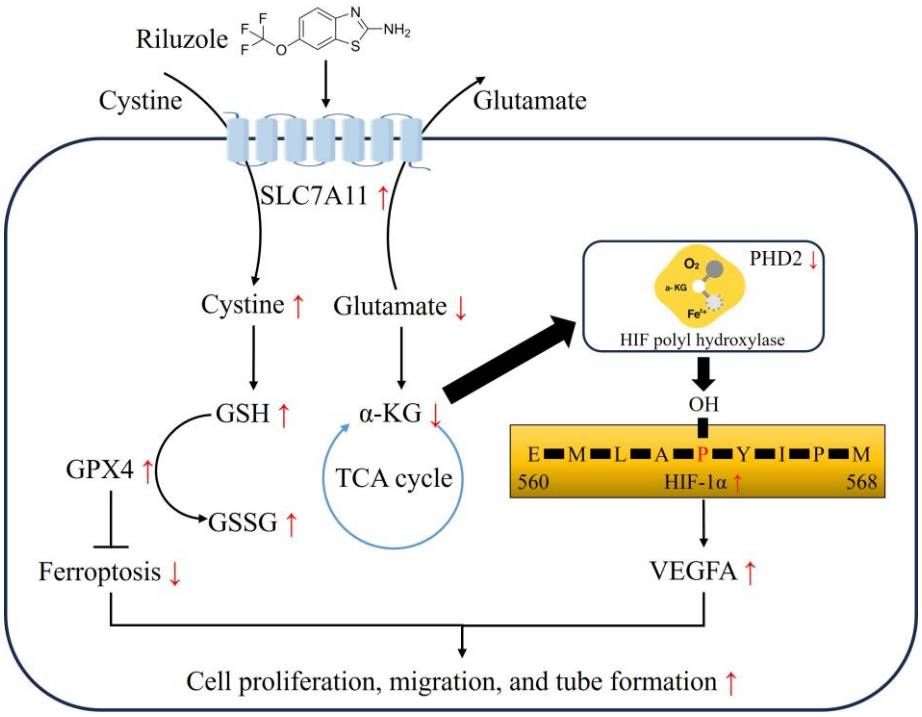

Fig. 9 Riluzole regulatory mechanism diagram.

Ethics approval

The management, use, and related operations of animals involved in this study were approved by the Institutional Animal Care and Use Committee (IACUC) of Huazhong University Agricultural Institution (Approval No. HZAUMO-2022-0203).

Consent for publication

All authors have approved of the consents of this manuscript and provided consent for publication.

Data availability

Sequencing data are available upon request to the corresponding author. Some data that support the findings of our study are openly available in the Gene Expression Omnibus (GSE303528) at https://www.ncbi.nlm.nih.gov/geo/.

Supplementary Materials

Supplementary Materials associated with this article, including Supplementary Figures S1-S11 and Supplementary Table S1, can be found in the online version.

Declaration of competing interest

The authors declare that they have no known competing financial interests or personal relationships that could have appeared to influence the work reported in this paper.

Funding

This study was supported by National Natural Science Foundation of China (Grant No. 32571174, 32400815), Hubei Provincial Natural Science Foundation (2025AFD036), the Key Project of Research and Development of Hubei Province (2022BCE049), Fundamental Research Funds for the Central Universities (2662022JC002).

CRediT authorship contribution statement

Haipeng Wang: Conceptualization, Data curation, Validation, Visualization, Methodology, Writing - original draft, Writing – review and editing. **Ying Feng:** Validation, Methodology. **Wei Jiang:** Validation, Methodology. **Han Wang:** Data curation, Visualization. **Ruolin Zhang:** Funding acquisition, Visualization. **Guangqiang Li:** Data curation, Investigation. **Chao Duan:** Data curation, Investigation. **Yuneng Zhou:** Data curation, Investigation. **Wendai Bao:** Conceptualization, Supervision. **Ke Shui:** Conceptualization, Supervision. **Min Zhang:** Resources, Formal analysis. **Zhibing Ai:** Resources. **Xin Yang:** Methodology, Writing – review and editing. **Peiyang Zhou:** Supervision, Investigation. **Zhiqiang Dong:** Conceptualization, Supervision, Funding acquisition, Writing - original draft, Writing – review and editing. All authors have read and agreed to the published version of the manuscript.

Acknowledgements

We thank the College of Biomedicine and Health, Huazhong Agricultural University for providing the experimental platform and conditions, and Dr. Xiangru Wang (Huazhong Agricultural University) for providing hBMECs.

620

621 **References**

622 [1] S. Paul, E. Candelario-Jalil, Emerging neuroprotective strategies for the treatment of ischemic
623 stroke: an overview of clinical and preclinical studies, Exp. Neurol. 335 (2021) 113518.

624 [2] J. Putaala, Ischemic stroke in young adults, Continuum (Minneap Minn) 26 (2) (2020) 386-
625 414.

626 [3] H.E. Marei, A. Hasan, R. Rizzi, A. Althani, N. Afifi, C. Cenciarelli, T. Caceci, A. Shuaib,
627 Potential of stem cell-based therapy for ischemic stroke, Front. Neurol. 9 (2018) 34.

628 [4] V.L. Feigin, M.H. Forouzanfar, R. Krishnamurthi, G.A. Mensah, M. Connor, D.A. Bennett,
629 A.E. Moran, R.L. Sacco, L. Anderson, T. Truelsen, M. O'Donnell, N. Venketasubramanian,
630 S. Barker-Collo, C.M. Lawes, W. Wang, Y. Shinohara, E. Witt, M. Ezzati, M. Naghavi, C.
631 Murray, Global and regional burden of stroke during 1990-2010: findings from the global
632 burden of disease study 2010, Lancet 383 (9913) (2014) 245-254.

633 [5] M.J. O'Donnell, S.L. Chin, S. Rangarajan, D. Xavier, L. Liu, H. Zhang, P. Rao-Melacini, X.
634 Zhang, P. Pais, S. Agapay, P. Lopez-Jaramillo, A. Damasceno, P. Langhorne, M.J. Mcqueen,
635 A. Rosengren, M. Dehghan, G.J. Hankey, A.L. Dans, A. Elsayed, A. Avezum, C. Mondo,
636 H.C. Diener, D. Ryglewicz, A. Czlonkowska, N. Pogosova, C. Weimar, R. Iqbal, R. Diaz,
637 K. Yusoff, A. Yusufali, A. Oguz, X. Wang, E. Penaherrera, F. Lanas, O.S. Ogah, A.
638 Ogunniyi, H.K. Iversen, G. Malaga, Z. Rumboldt, S. Oveisgharan, H.F. Al, D. Magazi, Y.
639 Nilanont, J. Ferguson, G. Pare, S. Yusuf, Global and regional effects of potentially
640 modifiable risk factors associated with acute stroke in 32 countries (INTERSTROKE): a
641 case-control study, Lancet 388 (10046) (2016) 761-775.

642 [6] Y. Hu, H. Lei, S. Zhang, J. Ma, S. Kang, L. Wan, F. Li, F. Zhang, T. Sun, C. Zhang, W. Li,
643 Panax notoginseng saponins protect brain microvascular endothelial cells against oxygen-
644 glucose deprivation/resupply-induced necroptosis via suppression of RIP1-RIP3-MLKL
645 signaling pathway, Neurochem. Res. 47 (11) (2022) 3261-3271.

646 [7] G. Cao, N. Jiang, Y. Hu, Y. Zhang, G. Wang, M. Yin, X. Ma, K. Zhou, J. Qi, B. Yu, J. Kou,
647 Ruscogenin attenuates cerebral ischemia-induced blood-brain barrier dysfunction by
648 suppressing TXNIP/NLRP3 inflammasome activation and the MAPK pathway, Int. J. Mol.
649 Sci. 17 (9) (2016).

[8] X. Jiang, A.V. Andjelkovic, L. Zhu, T. Yang, M. Bennett, J. Chen, R.F. Keep, Y. Shi, Blood-brain barrier dysfunction and recovery after ischemic stroke, Prog. Neurobiol. 163-164 (2018) 144-171.

[9] X. Wang, X. Yu, C. Xie, Z. Tan, Q. Tian, D. Zhu, M. Liu, Y. Guan, Rescue of brain function using tunneling nanotubes between neural stem cells and brain microvascular endothelial cells, Mol. Neurobiol. 53 (4) (2016) 2480-2488.

[10] W. Pan, Z. Xu, Triptolide mediates wnt/beta-catenin signalling pathway to reduce cerebral ischemia-reperfusion injury in rats, Folia Neuropathol. 58 (4) (2020) 324-333.

[11] F.L. Cardoso, D. Brites, M.A. Brito, Looking at the blood-brain barrier: molecular anatomy and possible investigation approaches, Brain Res Rev 64 (2) (2010) 328-363.

[12] S. Engelhardt, S.F. Huang, S. Patkar, M. Gassmann, O.O. Ogunshola, Differential responses of blood-brain barrier associated cells to hypoxia and ischemia: a comparative study, Fluids Barriers CNS 12 (2015) 4.

[13] G. Yang, N. Wang, S.W. Seto, D. Chang, H. Liang, Hydroxysafflor yellow a protects brain microvascular endothelial cells against oxygen glucose deprivation/reoxygenation injury: involvement of inhibiting autophagy via class i PI3k/akt/mTOR signaling pathway, Brain Res. Bull. 140 (2018) 243-257.

[14] X. Cheng, Z.U. Aabdin, Y. Wang, N. Ma, H. Dai, X. Shi, X. Shen, Glutamine pretreatment protects bovine mammary epithelial cells from inflammation and oxidative stress induced by gamma-d-glutamyl-meso-diaminopimelic acid (ie-DAP), J. Dairy. Sci. 104 (2) (2021) 2123-2139.

[15] Y.F. Ma, L. Zhao, D.N. Coleman, M. Gao, J.J. Loor, Tea polyphenols protect bovine mammary epithelial cells from hydrogen peroxide-induced oxidative damage in vitro by activating NFE2l2/HMOX1 pathways, J. Dairy. Sci. 102 (2) (2019) 1658-1670.

[16] Y. Wang, X. Zhang, Z. Wei, J. Wang, Y. Zhang, M. Shi, Z. Yang, Y. Fu, Platycodin d suppressed LPS-induced inflammatory response by activating LXRalpha in LPS-stimulated primary bovine mammary epithelial cells, Eur. J. Pharmacol. 814 (2017) 138-143.

[17] H. Ni, J. Li, J. Zheng, B. Zhou, Cardamonin attenuates cerebral ischemia/reperfusion injury by activating the HIF-1alpha/VEGFA pathway, Phytother. Res. 36 (4) (2022) 1736-1747.

[18] L. Wang, J. Li, Y. Wang, C. Ge, Q. Huang, L. Li, N. Wang, Y. Chen, X. Zhou, D. Chang, D.

Li, J. Hou, Dan-deng-tong-nao softgel capsule promotes angiogenesis of cerebral microvasculature to protect cerebral ischemia reperfusion injury via activating HIF-1alpha-VEGFA-notch1 signaling pathway, Phytomedicine 118 (2023) 154966.

[19] S.S. Shin, B.S. Jeong, B.A. Wall, J. Li, N.L. Shan, Y. Wen, J.S. Goydos, S. Chen, Participation of xCT in melanoma cell proliferation in vitro and tumorigenesis in vivo, Oncogenesis 7 (11) (2018) 86.

[20] L. Liu, Z. Zhao, Q. Yin, X. Zhang, TTB protects astrocytes against oxygen-glucose deprivation/reoxygenation-induced injury via activation of nrf2/HO-1 signaling pathway, Front. Pharmacol. 10 (2019) 792.

[21] C. Ge, D. Meng, Y. Peng, P. Huang, N. Wang, X. Zhou, D. Chang, The activation of the HIF-1alpha-VEGFA-notch1 signaling pathway by hydroxysafflor yellow a promotes angiogenesis and reduces myocardial ischemia-reperfusion injury, Int. Immunopharmacol. 142 (Pt A) (2024) 113097.

[22] S. Wu, B. Wu, M. Liu, Z. Chen, W. Wang, C.S. Anderson, P. Sandercock, Y. Wang, Y. Huang, L. Cui, C. Pu, J. Jia, T. Zhang, X. Liu, S. Zhang, P. Xie, D. Fan, X. Ji, K.L. Wong, L. Wang, Stroke in china: advances and challenges in epidemiology, prevention, and management, Lancet Neurol. 18 (4) (2019) 394-405.

[23] D. Barthels, H. Das, Current advances in ischemic stroke research and therapies, Biochim. Biophys. Acta-Mol. Basis Dis. 1866 (4) (2020) 165260.

[24] W. Abdullahi, D. Tripathi, P.T. Ronaldson, Blood-brain barrier dysfunction in ischemic stroke: targeting tight junctions and transporters for vascular protection, Am. J. Physiol. Cell Physiol. 315 (3) (2018) C343-C356.

[25] C.P. Profaci, R.N. Munji, R.S. Pulido, R. Daneman, The blood-brain barrier in health and disease: important unanswered questions, J. Exp. Med. 217 (4) (2020).

[26] J. Liu, Y. Sun, X. Zeng, Y. Liu, C. Liu, Y. Zhou, Y. Liu, G. Sun, M. Guo, Engineering and characterization of an artificial drug-carrying vesicles nanoplatform for enhanced specifically targeted therapy of glioblastoma, Adv. Mater. 35 (41) (2023) e2303660.

[27] Q.J. Yu, H. Tao, X. Wang, M.C. Li, Targeting brain microvascular endothelial cells: a therapeutic approach to neuroprotection against stroke, Neural Regen. Res. 10 (11) (2015) 1882-1891.

[28] X. Ji, J. Qian, S. Rahman, P.J. Siska, Y. Zou, B.K. Harris, M.D. Hoeksema, I.A. Trenary, C. Heidi, R. Eisenberg, J.C. Rathmell, J.D. Young, P.P. Massion, XCT (SLC7a11)-mediated metabolic reprogramming promotes non-small cell lung cancer progression, Oncogene 37 (36) (2018) 5007-5019.

[29] L. Sheng, Q. Luo, L. Chen, Amino acid solute carrier transporters in inflammation and autoimmunity, Drug. Metab. Dispos. (2022).

[30] W. Lin, C. Wang, G. Liu, C. Bi, X. Wang, Q. Zhou, H. Jin, SLC7a11/xCT in cancer: biological functions and therapeutic implications, Am. J. Cancer Res. 10 (10) (2020) 3106-3126.

[31] P. Koppula, Y. Zhang, L. Zhuang, B. Gan, Amino acid transporter SLC7a11/xCT at the crossroads of regulating redox homeostasis and nutrient dependency of cancer, Cancer Commun. 38 (1) (2018) 12.

[32] K. Hu, K. Li, J. Lv, J. Feng, J. Chen, H. Wu, F. Cheng, W. Jiang, J. Wang, H. Pei, P.J. Chiao, Z. Cai, Y. Chen, M. Liu, X. Pang, Suppression of the SLC7a11/glutathione axis causes synthetic lethality in KRAS-mutant lung adenocarcinoma, J. Clin. Invest. 130 (4) (2020) 1752-1766.

[33] G.H. Chen, C.C. Song, K. Pantopoulos, X.L. Wei, H. Zheng, Z. Luo, Mitochondrial oxidative stress mediated fe-induced ferroptosis via the NRF2-are pathway, Free. Radic. Biol. Med. 180 (2022) 95-107.

[34] X. Chen, J. Li, R. Kang, D.J. Klionsky, D. Tang, Ferroptosis: machinery and regulation, Autophagy 17 (9) (2021) 2054-2081.

[35] F. He, P. Zhang, J. Liu, R. Wang, R.J. Kaufman, B.C. Yaden, M. Karin, ATF4 suppresses hepatocarcinogenesis by inducing SLC7a11 (xCT) to block stress-related ferroptosis, J. Hepatol. 79 (2) (2023) 362-377.

[36] W. Zhang, Y. Sun, L. Bai, L. Zhi, Y. Yang, Q. Zhao, C. Chen, Y. Qi, W. Gao, W. He, L. Wang, D. Chen, S. Fan, H. Chen, H.L. Piao, Q. Qiao, Z. Xu, J. Zhang, J. Zhao, S. Zhang, Y. Yin, C. Peng, X. Li, Q. Liu, H. Liu, Y. Wang, RBMS1 regulates lung cancer ferroptosis through translational control of SLC7a11, J. Clin. Invest. 131 (22) (2021).

[37] X. Lang, M.D. Green, W. Wang, J. Yu, J.E. Choi, L. Jiang, P. Liao, J. Zhou, Q. Zhang, A. Dow, A.L. Saripalli, I. Kryczek, S. Wei, W. Szeliga, L. Vatan, E.M. Stone, G. Georgiou, M. Cieslik, D.R. Wahl, M.A. Morgan, A.M. Chinnaiyan, T.S. Lawrence, W. Zou, Radiotherapy

and immunotherapy promote tumoral lipid oxidation and ferroptosis via synergistic repression of SLC7a11, Cancer Discov. 9 (12) (2019) 1673-1685.

[38] Y. Long, H. Tao, A. Karachi, A.J. Grippin, L. Jin, Y.E. Chang, W. Zhang, K.A. Dyson, A.Y. Hou, M. Na, L.P. Deleyrolle, E.J. Sayour, M. Rahman, D.A. Mitchell, Z. Lin, J. Huang, Dysregulation of glutamate transport enhances treg function that promotes VEGF blockade resistance in glioblastoma, Cancer Res. 80 (3) (2020) 499-509.

[39] V.H. Villar, F. Merhi, M. Djavaheri-Mergny, R.V. Duran, Glutaminolysis and autophagy in cancer, Autophagy 11 (8) (2015) 1198-1208.

[40] S. Raffel, M. Falcone, N. Kneisel, J. Hansson, W. Wang, C. Lutz, L. Bullinger, G. Poschet, Y. Nonnenmacher, A. Barnert, C. Bahr, P. Zeisberger, A. Przybylla, M. Sohn, M. Tonjes, A. Erez, L. Adler, P. Jensen, C. Scholl, S. Frohling, S. Cocciardi, P. Wuchter, C. Thiede, A. Florcken, J. Westermann, G. Ehninger, P. Lichter, K. Hiller, R. Hell, C. Herrmann, A.D. Ho, J. Krijgsveld, B. Radlwimmer, A. Trumpp, BCAT1 restricts alphaKG levels in AML stem cells leading to IDHmut-like DNA hypermethylation, Nature 551 (7680) (2017) 384-388.

[41] Q. He, M. Liu, W. Huang, X. Chen, B. Zhang, T. Zhang, Y. Wang, D. Liu, M. Xie, X. Ji, M. Sun, D. Tian, L. Xia, IL-1beta-induced elevation of solute carrier family 7 member 11 promotes hepatocellular carcinoma metastasis through up-regulating programmed death ligand 1 and colony-stimulating factor 1, Hepatology. 74 (6) (2021) 3174-3193.

[42] J. Tao, R. Miao, G. Liu, X. Qiu, B. Yang, X. Tan, L. Liu, J. Long, W. Tang, W. Jing, Spatiotemporal correlation between HIF-1alpha and bone regeneration, Faseb. J. 36 (10) (2022) e22520.

[43] R. Chen, J.E. Liliental, P.E. Kowalski, Q. Lu, S.N. Cohen, Regulation of transcription of hypoxia-inducible factor-1alpha (HIF-1alpha) by heat shock factors HSF2 and HSF4, Oncogene 30 (22) (2011) 2570-2580.

[44] R. Wei, L. Song, Z. Miao, K. Liu, G. Han, H. Zhang, D. Ma, J. Huang, H. Tian, B. Xiao, C. Ma, Hydroxysafflor yellow a exerts neuroprotective effects via HIF-1alpha/BNIP3 pathway to activate neuronal autophagy after OGD/r, Cells 11 (23) (2022).

[45] C. Heurteaux, C. Laigle, N. Blondeau, G. Jarretou, M. Lazdunski, Alpha-linolenic acid and riluzole treatment confer cerebral protection and improve survival after focal brain ischemia, Neuroscience 137 (1) (2006) 241-251.

[46] A.Y. Liu, R. Mathur, N. Mei, C.G. Langhammer, B. Babiarz, B.L. Firestein, Neuroprotective drug riluzole amplifies the heat shock factor 1 (HSF1)- and glutamate transporter 1 (GLT1)-dependent cytoprotective mechanisms for neuronal survival, J. Biol. Chem. 286 (4) (2011) 2785-2794.

[47] R. Taiji, M. Yamanaka, W. Taniguchi, N. Nishio, S. Tsutsui, T. Nakatsuka, H. Yamada, Anti-allodynic and promotive effect on inhibitory synaptic transmission of riluzole in rat spinal dorsal horn, Biochem. Biophys. Rep. 28 (2021) 101130.

[48] G.M.I. Chowdhury, M. Banasr, R.A. de Graaf, D.L. Rothman, K.L. Behar, G. Sanacora, Chronic riluzole treatment increases glucose metabolism in rat prefrontal cortex and hippocampus, J. Cereb. Blood. Flow. Metab. 28 (12) (2008) 1892-1897.

[49] R.S. Baker, J.T. Wang, N. Rouatbi, Y. Lu, T. Al-Adhami, D. Asker, K.M. Rahman, A. Al-Chalabi, B. Forbes, S. Bansal, K.T. Al-Jamal, Brain distribution study of [(14)c]-riluzole following intranasal administration in mice, Int. J. Pharm. 670 (2025) 125195.

[50] X. Liu, L. Nie, Y. Zhang, Y. Yan, C. Wang, M. Colic, K. Olszewski, A. Horbath, X. Chen, G. Lei, C. Mao, S. Wu, L. Zhuang, M.V. Poyurovsky, Y.M. James, T. Hart, D.D. Billadeau, J. Chen, B. Gan, Actin cytoskeleton vulnerability to disulfide stress mediates disulfidptosis, Nat. Cell Biol. 25 (3) (2023) 404-414.

[51] Y. Xu, Y. Li, J. Li, W. Chen, Ethyl carbamate triggers ferroptosis in liver through inhibiting GSH synthesis and suppressing nrf2 activation, Redox Biol. 53 (2022) 102349.

[52] B. Zhang, W. Bao, S. Zhang, B. Chen, X. Zhou, J. Zhao, Z. Shi, T. Zhang, Z. Chen, L. Wang, X. Zheng, G. Chen, Y. Wang, LncRNA HEPFAL accelerates ferroptosis in hepatocellular carcinoma by regulating SLC7a11 ubiquitination, Cell Death Dis. 13 (8) (2022) 734.

[53] H. Feng, Q. Liu, Z. Deng, H. Li, H. Zhang, J. Song, X. Liu, J. Liu, B. Wen, T. Wang, Human umbilical cord mesenchymal stem cells ameliorate erectile dysfunction in rats with diabetes mellitus through the attenuation of ferroptosis, Stem Cell Res. Ther. 13 (1) (2022) 450.